Multi-objective optimization for dimensional synthesis of tendon placement and structural design for energy-efficient and feasible static workspace in continuum robots

Original
Multi-objective optimization for dimensional synthesis of tendon placement and structural design for energy-efficient and feasible static workspace in continuum robots / Jabari, M., Visconte, C., Quaglia, G., Laribi, M.A.. - In: ROBOTICS AND AUTONOMOUS SYSTEMS. - ISSN 0921-8890. - 197:(2026). [10.1016/j.robot.2025.105300]

Publisher:
Elsevier

Published
DOI:10.1016/j.robot.2025.105300

Robotics and Autonomous Systems 197 (2026) 105300

Contents lists available at ScienceDirect

Robotics and Autonomous Systems

journal homepage: www.elsevier.com/locate/robot

Multi-objective optimization for dimensional synthesis of tendon placement and structural design for energy-efficient and feasible static workspace in continuum robots

Mohammad Jabari [a,b,*], Carmen Visconte [b], Giuseppe Quaglia [b], Med Amine Laribi [c]

[a] Department of Informatics, Bioengineering, Robotics and Systems Engineering (DIBRIS), Università di Genova, Genova, Italy
[b] Department of Mechanical and Aerospace Engineering, Politecnico di Torino, Corso Duca degli Abruzzi 24, Turin 10129, Italy
[c] Department of GMSC, Pprime Institute, University of Poitiers, CNRS, ISEA-ENSMA, UPR 3346, Poitiers, France

ARTICLE INFO

Keywords:
Continuum robots
Tendon-driven actuation
Kineto-static modeling
Multi-objective optimization
Feasible static workspace

ABSTRACT

Tendon-driven continuum robots (TDCRs) face a critical trade-off between energy efficiency and static performance for navigating constrained environments, a challenge in medical and industrial applications. This study proposes a bi-objective optimization framework to enhance tendon placement and dimensional synthesis in a two-segment TDCR, featuring seven disks and four tendons per segment. Leveraging a kineto-static model based on piecewise constant curvature (PCC) theory and a multi-objective genetic algorithm (MOGA), radial tendon distances and angular offsets have been optimized. These solutions achieve up to 30 % reduction in mechanical work and a 3–5 % workspace expansion, validated through 100 randomized tendon force samples. The results offer practical guidelines for improving TDCR performance in both minimally invasive surgery and industrial inspection.

1. Introduction

Continuum robots, characterized by their infinite degrees of freedom and bioinspired compliance, have emerged as transformative tools in fields ranging from minimally invasive surgery to industrial inspection [1–3]. Their ability to navigate confined spaces stems from their continuous backbone, which deforms through tendon-driven actuation systems. Early designs, such as Anderson’s tensor arm, laid the groundwork for tendon-driven continuum robots (TDCRs), while modern innovations now integrate hybrid actuation, modular architectures, and advanced materials to enhance precision and adaptability [4]. A critical challenge in TDCR design lies in optimizing structural parameters such as backbone stiffness, tendon routing, and segment modularity to balance energy efficiency, workspace performance, and geometric feasibility [5].

The evolution of TDCR structural design has been marked by different approaches. The piecewise constant curvature (PCC) assumption, popularized by Webster and Jones [5], simplifies kinematics by approximating backbone segments as constant-curvature arcs but struggles with torsional and dynamic effects . Recent work by Starke et al. [6] demonstrated that helical tendon routing expands workspace volume fourfold compared to straight configurations, though this introduces challenges in managing torsional stability and friction. Concurrently, Amanov et al. [7] highlighted trade-offs between segment extensibility and actuation complexity, showing that variable-length segments improve follow-the-leader deployment but require intricate structural co-design.

Structural optimization frameworks increasingly emphasize geometric constraints and tendon non-interference. Grassmann et al. [8] established radial separation thresholds (e.g., $\Delta r \geq 1$ mm) and angular spacing limits ($\alpha \geq 30^\circ$) to prevent tendon collisions in multi-segment designs. For instance, spacer disk configurations either fixed (Type-0) or floating (Type-III) significantly influence tendon routing efficiency and backbone deformation [9]. Modular designs, such as those proposed by Barrientos-Diez et al. [10], leverage asymmetric backbone architectures to enhance workspace uniformity and reduce actuation forces by 15–22 % compared to symmetric layouts.

The integration of additive manufacturing has further advanced structural optimization. Perugini and Russo [11] introduced a monolithic 3D-printed TDCR design, eliminating the need for discrete spacer

---

* Corresponding author.
E-mail addresses: mohammad.jabari@polito.it (M. Jabari), carmen.visconte@polito.it (C. Visconte), giuseppe.quaglia@polito.it (G. Quaglia), med.amine.laribi@univ-poitiers.fr (M.A. Laribi).

https://doi.org/10.1016/j.robot.2025.105300
Received 4 June 2025; Received in revised form 8 December 2025; Accepted 10 December 2025

disks by embedding tendon lumens directly into a flexible backbone. This approach reduces assembly complexity while maintaining accuracy comparable to traditional multi-component designs . Similarly, FDM-printable designs with serial S-shaped backbones, as proposed by recent studies, enable planar bending with minimized plastic deformation, demonstrating the viability of cost-effective prototyping for complex geometries.

Increasing the number of segments introduces both opportunities and challenges. Multi-segment TDCRs, as demonstrated by Dong et al. [12], achieve enhanced reachability in extreme environments (e.g., aircraft engine repair at 2000 °C) but face trade-offs in tendon density and friction management . For example, a two-segment robot with 4 tendons per segment achieves a 32 % larger workspace than single-segment counterparts, yet asymmetric radial placement (proximal: 6.5 mm, distal: 3.5 mm) is necessary to mitigate mechanical work increases [10]. Configurable tendon routing, as explored by Barreiros et al. [9], enables spatial follow-the-leader deployment but requires robust optimization frameworks to handle nonlinear constraints .

Material selection remains pivotal in structural optimization. Backbones composed of nested concentric tubes or laser-patterned polymers [13] allow variable stiffness profiles, while monolithic 3D-printed designs prioritize manufacturability and reproducibility. For instance, Grassmann et al. [14] advocate for open-source modular platforms to standardize benchmarking, noting that 61 % of TDCR prototypes are abandoned due to irreproducible designs. Bottcher et al. [15] demonstrated that coupling three tendon-actuated continuum robots at a common end-effector platform improves position repeatability by 67 %, showcasing the benefits of parallel architectures in precision-critical applications . Similarly, Kato et al. [16] developed a two-section TDCR for endoscopic surgery, incorporating friction-aware kinematic mapping to enhance tip positioning accuracy under large bending angles, achieving errors below 6 mm .

Computational modeling plays an indispensable and profoundly significant role in the domain of structural design. Runge et al. [17] emphasized the need for high-fidelity finite element analysis (FEA) to train machine learning surrogates, enabling rapid design iterations while accounting for nonlinear material behavior . Wang et al. [18] further validated FEA-driven stability analyses, identifying optimal slenderness ratios to prevent buckling in miniature spring-based manipulators .

The field of continuum robotics is progressing from foundational kinematic formulations toward advanced co-design frameworks that integrate geometric constraints, material properties, and tendon routing. Previous studies have achieved notable results in areas such as workspace expansion [6,10,19,20], structural stability [18,21], and manufacturability via monolithic designs [11]. However, most of these works rely on single-objective optimization, focusing either on workspace maximization or simplified fabrication without addressing the coupled trade-off between energy efficiency and static performance under nonlinear geometric constraints. In contrast, the objectives of this research are twofold: (1) establish a robust bi-objective optimization framework that minimizes mechanical work while maximizing the feasible static workspace under nonlinear geometric constraints, and (2) derive actionable design guidelines for asymmetric tendon arrangements and modular segment configurations that balance performance and manufacturability. To address this problem, a Pareto-based multi-objective genetic algorithm (MOGA) is used, inspired by evolutionary processes including selection, crossover, and mutation [23].

This paper represents a substantial extension of the earlier conference publication. The conference paper focused solely on a single-objective optimization problem in which tendon forces were the only design variables used to maximize the feasible static workspace (FSW) under external loads. In contrast, the present manuscript introduces a fundamentally expanded formulation in both methodology and design scope. First, a bi-objective optimization framework is proposed that simultaneously minimizes mechanical work and maximizes FSW using MOGA/NSGA-II. Second, the design variables are expanded to include structural parameters namely the tendon radial distances (r_1, r_2) and the inter-segment angular offset (α) subject to nonlinear geometric and non-interference constraints. Third, a statistically robust evaluation based on 100 randomized tendon-force samples is incorporated, together with detailed Pareto analyses (Figs. 7–17) and the derivation of actionable design guidelines (e.g., $r_1 = 21$ mm, $r_2 = 22.5$ mm, $\alpha = 45^\circ$). Altogether, these additions deliver a substantially more comprehensive and generalizable optimization framework compared with the preliminary findings presented in the previous work [20].

2. Two-Segment tendon-driven continuum robot (TDCR)

The design of tendon-driven continuum robots is particularly challenging due to their high-dimensional kinematics and the inherent fragility of the tendon actuation mechanism. These robots typically comprise numerous vertebrae linked by a flexible backbone and actuated by tendons. Fig. 1 shows a conceptual schematic of a two-segment TDCR, including 7 vertebrae per segment and driven by two sets of tendon actuators. Fig. 2(a) depicts the CAD model of robot, where each segment is equipped with four tendons. The tendon anchor points in Segment 1 are shown in Fig. 2(b), and the spatial distribution of tendons around the vertebral surface is detailed in Fig. 2(c). A close-up view of the compliant intervertebral joint is presented in Fig. 2(d), while Fig. 2 (e) shows the assembled prototype mounted at the end of a serial IGUS® robotic arm for experimentation. The prototype consists of a rigid actuation module containing two Dynamixel® 2XC 430-W250-T servomotors that drive four pairs of orthogonally arranged, antagonistic steel tendons (0.5 mm in diameter). Each tendon is actuated using a motor-driven pulley mechanism, where the pulley 's rotation angle defines tendon displacement and controls segment bending. The TDCR structure itself is a monolithic one, fabricated from 3D-printed PA12 Nylon® using selective laser sintering (SLS), and contains 7 vertebrae per segment with compliant joints that emulate natural bending motions.

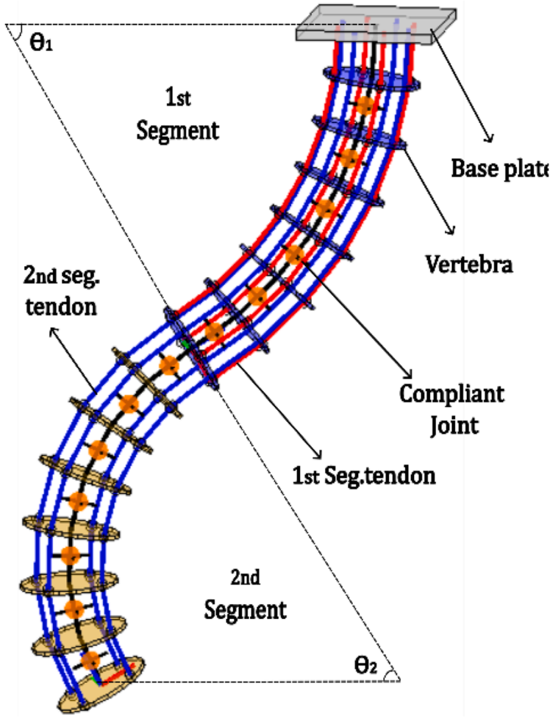

Fig. 1. Four-tendon arrangement on the disc of each section of the two-segment robot.

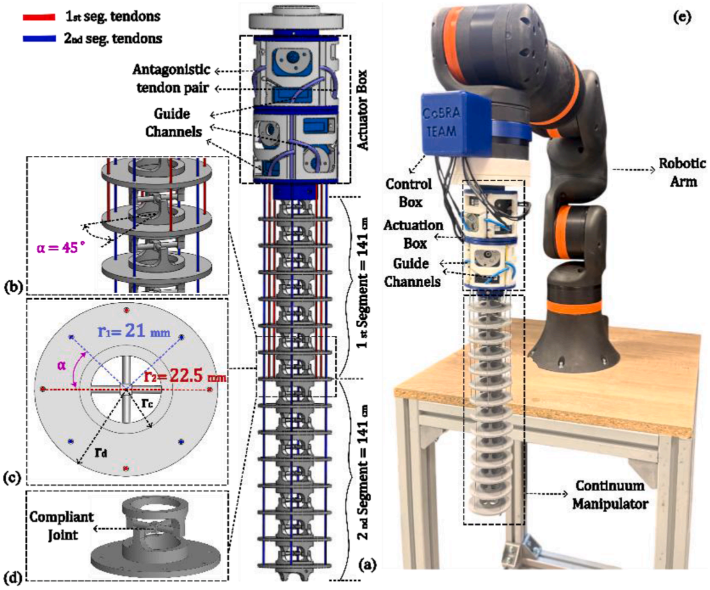

Fig. 2. (a) CAD schematic of a two-segment, TDCR with four tendons in each segment (b) Anchor points for the tendons in Segment 1 (c) Distribution of tendons on the surface of the vertebra (d) Compliant joint (e) Actual prototype.

2.1. *Geometric modeling of a representative vertebra for optimization*

Fig. 3 illustrates the tendon layout on a representative vertebra, which serves as the geometric foundation for the optimization framework. Each segment includes four tendons arranged symmetrically at radial distances r_1 and r_2 from the vertebral center, with an angular offset α between the starting positions of each segment's tendons. Additional geometric parameters such as tendon channel diameters (d_1, d_2) and the vertebral, backbone radii (r_d, r_c) are also considered.

The local position of tendon c in segment m (with $m = 1,2$) is defined in the local coordinate frame of the vertebra as [24]:

$$^{i}\boldsymbol{p}_{i,c} = r_m[\cos(\delta_{m,c}) \quad \sin(\delta_{m,c}) \quad 0], \; c = 1,2,3,4 \tag{1}$$

where $\delta_{m,c} = 2\pi(c-1)/4 + \delta_m$ with $\delta_1 = 0, \delta_2 = \alpha$. Here, r_m denotes the radial tendon distance in segment m, corresponding to either r_1 and r_2 in the first and second segments, respectively (see Fig. 3).

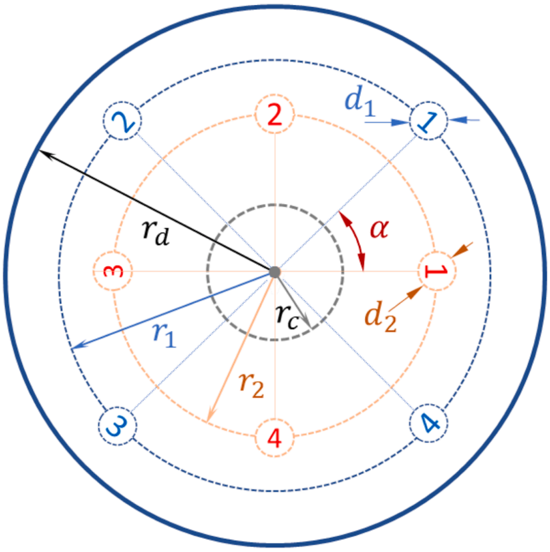

Fig. 3. Four-tendon arrangement on the disc of each section of the two-segment robot.

This formulation captures the symmetrical tendon arrangement in each segment and the angular offset between segments. These variables define the core design space for optimization and the modeling of geometric constraints.

3. Kineto-static modeling of TDCR

To capture the static deformation behaviour of the TDCR, a kineto-static model based on the piecewise constant curvature (PCC) assumption is employed [24] . This model estimates the robot's static equilibrium configuration in response to applied tendon forces, enabling evaluation of resulting tip poses and mechanical work. A tendon force vector $\boldsymbol{F} \in \mathbb{R}^8$ is defined, where each corresponds to one of the eight tendons (four per segment). To explore the range of static configurations the robot can achieve, a set of 100 force vectors $\{\boldsymbol{F_i}\}$ is randomly generated, with elements sampled from a normal distribution $\boldsymbol{F_i} \sim \mathcal{N}(0, \sigma^2)$ (N) with $\sigma = 0.5$. For each force vector $\boldsymbol{F_i}$, the kineto-static model solves the equilibrium shape and calculates the corresponding end-effector pose and total mechanical work. This provides a set of reachable configurations under passive tendon loading, independent on specific actuation policies. As shown in Fig. 5, the distribution of tip positions resulting from these force samples demonstrates that tendon force variation alone is sufficient to span a representative region of the robot's feasible static workspace. Importantly, these force samples are held constant during the optimization process. Design candidates are evaluated under the same set of force conditions to ensure consistent and reproducible performance comparison across configurations.

3.1. *Kinematic modeling of TDCR*

In the kinematic modeling of the TDCR, the (PCC) assumption is applied, meaning that each segment bends with a locally constant curvature [24]. This assumption simplifies the robot's geometry by modeling each segment as a circular arc with fixed curvature and twist.

Fig. 6(a) illustrates a section of the robot comprising consecutive vertebrae, two sample tendons, local coordinate frames, and the forces acting on the backbone and vertebrae. Fig. 6(b) shows a magnified view of a universal joint connecting the backbone to each vertebra, along with curvature angle notations that define the configuration of the robot components. Fig. 6(c) and (e) depict internal forces and tendon tensions acting on disk i, transmitted from disks $i+1$ and $i-1$, respectively.

The position $\boldsymbol{d}(\boldsymbol{s}_i)$ of any point along the arc, expressed in the frame of vertebra $i-1$, is given by [23,24]:

$$\boldsymbol{d}(\boldsymbol{s}_i) = \begin{bmatrix} \boldsymbol{x}_i \\ \boldsymbol{y}_i \\ \boldsymbol{z}_i \end{bmatrix} = \begin{bmatrix} \cos(\phi_i)(1-\cos(\boldsymbol{\theta}(\boldsymbol{s}_i))/\boldsymbol{k}_i \\ \sin(\phi_i)(1-\cos(\boldsymbol{\theta}(\boldsymbol{s}_i))/\boldsymbol{k}_i \\ \boldsymbol{sin}(\boldsymbol{\theta}_i)/\boldsymbol{k}_i \end{bmatrix} \tag{2}$$

The subsegment curvature k_i is defined by (3) [24,25],

$$k(s_i) = \sqrt{\beta_i^2 + \Gamma_i^2} \tag{3}$$

where β_i and Γ_i are the curvature of backbone along $\overrightarrow{\boldsymbol{x}}_{i-1}$ and $\overrightarrow{\boldsymbol{y}}_{i-1}$, and ϕ_i is defined as Eq. (3)[24]:

$$\phi_i = \tan^{-1}(\Gamma_i,\ \beta_i) \tag{4}$$

Given d_i for $s_i = l_i$, the homogeneous transformation matrix from $i-1$ to i is given by [24]:

$$^{i-1}T_i = \begin{bmatrix} R_z(\phi_i)R_y(\theta_i)R_z(-\phi_i) & d_i \\ 0 & 1 \end{bmatrix} \tag{5}$$

The direct geometrical model links the actuator space, giving the pulley angles, to the configuration space and to the cartesian space at the robot tip [24].

3.2. Static modeling of TDCR

The static behavior of the TDCR is governed by a force and moment balance under the assumption of (PCC). Based on this model, the bending deformation and tip position can be predicted by solving a set of nonlinear equilibrium equations derived from applied loads, tendon tensions, and elastic reactions.

Under the quasi-static assumption, the robot is influenced by gravitational forces, frictional interactions, external loads, and tendon tensions. Each of these contributions is transformed into the local coordinate frame for analysis. The gravitational force acting on the $(i)^{th}$ disk in the local frame is:

$$^{i-1}\boldsymbol{F}_{\boldsymbol{d},i} = {}^{i-1}T_0\,{}^0F_{d,i} \tag{6}$$

in which the gravity force $^0\boldsymbol{F}_{\boldsymbol{d},\boldsymbol{i}}$ is given as:

$$^0\boldsymbol{F}_{\boldsymbol{d},i} = [\,0 \quad 0 \quad -m_{d,i}.g \quad 0\,]^T \tag{7}$$

where $m_{d,i}$ is the disk's mass, g is gravitational acceleration, and $^{i-1}T_0$ is the transformation matrix to the local frame.

Similarly, the gravity acting on the backbone segment is:

$$^{i-1}\boldsymbol{F}_{\boldsymbol{b},i} = {}^{i-1}T_0\,{}^0\boldsymbol{F}_{\boldsymbol{b},i} \tag{8}$$

in which the gravity force $^0\boldsymbol{F}_{\boldsymbol{b},i}$ is given as:

$$^0F_{b,i} = [\,0 \quad 0 \quad -m_{b,i}.g \quad 0\,]^T \tag{9}$$

in which $m_{b,i}$ is the backbone's mass of $(i)^{th}$ disk.

The resulted moment of gravity forces on the disks and part of backbone are described as [24]:

$$^{i-1}\boldsymbol{M}_{\boldsymbol{d},i} = \left(\overrightarrow{^{i-1}o_{i-1}\,{}^{i-1}o_i}\right) \times \left({}^{i-1}\boldsymbol{F}_{\boldsymbol{d},i}\right) \tag{10}$$

$$^{i-1}\boldsymbol{M}_{\boldsymbol{b},i} = \left(\overrightarrow{^{i-1}o_{i-1}\,{}^{i-1}\boldsymbol{p}_{\boldsymbol{b},i-1}}\right) \times \left({}^{i-1}\boldsymbol{F}_{\boldsymbol{b},i}\right) \tag{11}$$

in which $^{i-1}o_{i-1}$, $^{i-1}o_i$ and $^{i-1}\boldsymbol{p}_{\boldsymbol{b},\boldsymbol{i}-1}$ represent the coordinates of the center of $(i-1)^{th}$ and $(i)^{th}$ disks, and the center of gravity of the backbone between $(i-1)^{th}$and $(i)^{th}$ disks in $(i-1)$ local frame, respectively.

In the case of interaction between TDCR and the surrounding environment, the external force $\boldsymbol{F}_{\boldsymbol{ext}}$ and torque $\boldsymbol{M}_{\boldsymbol{ext}}$ applied to the robot tip, denoted by index ν, and expressed in the tip coordinates, are described by the following relations [23]:

$$^{\nu-1}\boldsymbol{F}_{\boldsymbol{ext}} = {}^{\nu-1}T_0\,{}^0\boldsymbol{F}_{\boldsymbol{ext}} \tag{12}$$

$$^{\nu-1}\boldsymbol{M}_{\boldsymbol{ext}} = \left(\overrightarrow{^{\nu-1}o_{\nu-1}\,{}^{\nu-1}o_\nu}\right) \times \left({}^{\nu-1}\boldsymbol{F}_{\boldsymbol{ext}}\right) \tag{13}$$

where $^0\boldsymbol{F}_{\boldsymbol{ext}}$ is the force applied to the robot tip in the inertial frame.

Directional unit vectors as defined as below:

$$\overrightarrow{^{i-1}\boldsymbol{U}_{i-1,c}} = \frac{\overrightarrow{^{i-1}\boldsymbol{p}_{i,c}\,{}^{i-1}\boldsymbol{p}_{i-1,c}}}{\left\|\overrightarrow{^{i-1}\boldsymbol{p}_{i,c}\,{}^{i-1}\boldsymbol{p}_{i-1,c}}\right\|} \tag{14}$$

$$\overrightarrow{^{i-1}\boldsymbol{U}_{i+1,c}} = \frac{\overrightarrow{^{i-1}\boldsymbol{p}_{i,c}\,{}^{i-1}\boldsymbol{p}_{i+1,c}}}{\left\|\overrightarrow{^{i-1}\boldsymbol{p}_{i,c}\,{}^{i-1}\boldsymbol{p}_{i+1,c}}\right\|} \tag{15}$$

here, $\boldsymbol{p}_{i,c}$ and $\boldsymbol{p}_{i-1,c}$ denote the position of tendon c on disks (i) and $(i-1)$, respectively, expressed in the coordinate frame of disk $(i-1)$.

The driving tendon tension $^{i-1}\boldsymbol{F}_{\boldsymbol{i},\boldsymbol{c}}$ is the resultant of the two force vectors $\boldsymbol{F}_{i,c}$ and $\boldsymbol{F}_{i+1,c}$ by tendon c illustrated in Fig. 6(b), which are expressed using their unit direction vectors as below [24]:

$$^{i-1}\boldsymbol{F}_{i,c} = \boldsymbol{F}_{i,c}\overrightarrow{^{i-1}\boldsymbol{U}_{i-1,c}} + \boldsymbol{F}_{i+1,c}\overrightarrow{^{i-1}\boldsymbol{U}_{i+1,c}} \tag{16}$$

$$^{i-1}\boldsymbol{M}_{i,c} = \overrightarrow{^{i-1}\boldsymbol{p}_{i,c}} \times \left({}^{i-1}\boldsymbol{F}_{i,c}\right) \tag{17}$$

The motion of the robot along its path is driven by the forces exerted by the tendons. As the robot's configuration changes, frictional forces arise at the contact points between the tendons and the corresponding discs. These frictional forces are transmitted from the tendons to the discs and are calculated using the following equation.

The coefficient of friction is given as [24]

$$\mu_{i,c} = 0.689e^{-0.027\sigma_{i,c}} \tag{18}$$

in which $\sigma_{i,c}$ is the local bending angle of the vertebrae determined using directional unit vectors as below:

$$\sigma_{i,c} = \cos^{-1}\left({}^{i-1}\boldsymbol{U}_{i-1,c}\ .\,{}^{i-1}\boldsymbol{U}_{i+1,c}\right) \tag{19}$$

The tension magnitude $\boldsymbol{F}_{i+1_c}$ is updated applying friction force between the disks and the tendons.

$$\boldsymbol{F}_{i+1_c} = \boldsymbol{F}_{i_c} - \mu_{i,c}\left|{}^{i-1}\boldsymbol{N}_{i,c}\right| \tag{20}$$

$^{i-1}\boldsymbol{N}_{\boldsymbol{i},\boldsymbol{c}}$ is the normal force applied by tendon tension on the associated disk plane, which is computed using following relation [24]:

$$^{i-1}\boldsymbol{N}_{i,c} = {}^{i-1}\boldsymbol{F}_{i,c} - \left({}^{i-1}\boldsymbol{F}_{i,c}.{}^{i-1}\boldsymbol{n}_i\right) \tag{21}$$

where $^{i-1}\boldsymbol{n}_{\boldsymbol{i}}$ is the unit normal vector of plane (O_i, x_i, y_i).

The backbone of the TDCR is modeled as an elastic rod with the capability to undergo lateral bending and torsion. Let K_i denote the curvature and ε_i the torsional twist of the $(i)^{th}$ segment. The bending and torsional moments are computed based on material and geometric properties Young's modulus E, shear modulus G, second moment of area I, polar moment of inertia J, and segment length l_i. The resulting expressions for bending and torsional moments in the local frame are: [24, 25]:

$$^{i-1}\boldsymbol{M}_{b,i} = {}^{i-1}T_i[\,0 \quad E.I.K_i \quad 0 \quad 0\,]^T \tag{22}$$

$$^{i-1}\boldsymbol{M}_{\tau,i} = {}^{i-1}T_i[\,0 \quad 0 \quad G.J.(\varepsilon_i/l_i) \quad 0\,]^T \tag{23}$$

3.2.1. Equilibrium equations

The equilibrium behavior of the TDCR is governed by the recursive Newton–Euler equations, which balance all forces and moments acting on each vertebra in its local coordinate frame [25,26]. These equations are expressed as:

$$ {}^{i-1}\boldsymbol{F}_{O_{i-1}} = \sum_{k=1}^{c} {}^{i-1}\boldsymbol{F}_{i,k} + {}^{i-1}\boldsymbol{F}_{d,i} + {}^{i-1}\boldsymbol{F}_{b,i} + {}^{i-1}\boldsymbol{F}_{O_i} \tag{24} $$

$$ {}^{i-1}\boldsymbol{M}_{O_{i-1}} = \sum_{k=1}^{c} {}^{i-1}\boldsymbol{M}_{i,k} + {}^{i-1}\boldsymbol{M}_{d,i} + {}^{i-1}\boldsymbol{M}_{b,i} + {}^{i-1}\boldsymbol{M}_{O_i} \tag{25} $$

The discretized forces and moments ${}^{i-1}\boldsymbol{F}_{O_i}$ and ${}^{i-1}\boldsymbol{M}_{O_i}$ are the lumped forces and moments at point O_i in the frame $(i\ -\ -1)$ [24].

Eq. (25) expresses the static moment equilibrium for each vertebra of the TDCR, accounting for contributions from tendon-induced moments, distributed external loads, and internal elastic reactions. The elastic deformation of the backbone due to bending and torsion is governed by the constitutive relations in Eqs. (22) and (23), which relate bending and torsional moments to curvature and twist under small-strain linear elasticity. Eq. (26) combines these internal elastic moments to complete the moment balance.

$$ {}^{i-1}\boldsymbol{M}_{O_{i-1}} = {}^{i-1}\boldsymbol{M}_{b,i} + {}^{i-1}\boldsymbol{M}_{\tau,i} \tag{26} $$

By solving the above nonlinear coupled equations, the static configuration of the TDCR is determined [24].

4. Dimensional synthesis of TDCRs

This section presents the formulation of the dimensional synthesis problem for tendon-driven continuum robots (TDCRs). The objective is to determine optimal tendon routing parameters that achieve a balance between mechanical energy efficiency and feasible static workspace coverage, while satisfying geometric and physical constraints.

To this end, we consider three primary design variables $\xi = [r_1, r_2, \alpha]^T$ which (r_1, r_2) are the radial tendon distances in each segment and α is the angular offset between the tendon layouts of adjacent segments. These geometric parameters define the tendon routing configuration and directly influence both energy efficiency and the extent of the feasible static workspace.

A critical geometric constraint, known as tendon non-interference, ensures that tendons remain sufficiently spaced and avoid collision with one another or with the backbone during bending. As illustrated in Fig. 4, this constraint is formulated as a nonlinear inequality based on the spatial relationship among, (r_1, r_2) and α, and is evaluated across the admissible configuration space to guarantee physically feasible, collision-free designs (see. Section 4.3). The bi-objective nature of the problem is captured the bi-objective optimization framework, as described in the following subsections.

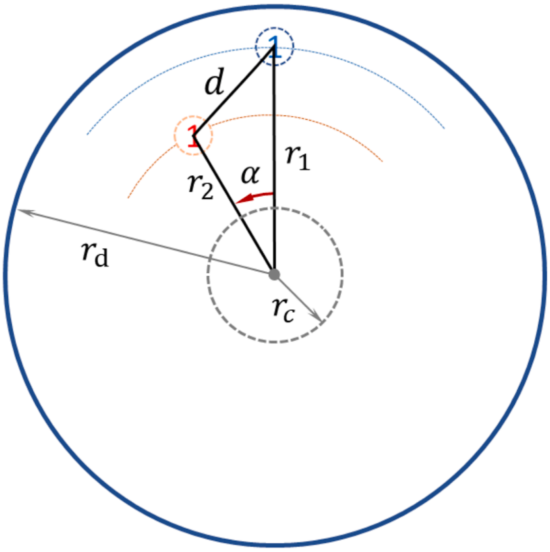

Fig. 4. Geometric constraint ensuring minimum tendon spacing.

4.1. *Formulation of the optimization problem*

The dimensional synthesis of TDCRs involves determining design parameters that minimize the mechanical work required for actuation while maximizing the feasible static workspace. These two competing objectives must be optimized simultaneously under nonlinear geometric constraints.

There are two general approaches to multiple-objective optimization. One is to combine the individual objective functions into a single composite function by normalizing them and using weighted combination approaches, so to find a single final solution. This can be considered a priori approach: the result is a consequence of pre-defined preferences expressed when defining the weights, which may not fully capture the diversity of available solutions. The second general approach is a posteriori decision-making method, which applies the Pareto-dominance approach to the objective function values. This way, an entire set of Pareto-optimal trade-offs, which provide flexible design guidelines adaptable to task-specific requirements, is found. Typical application scenarios include minimally invasive or endoscopic surgery, where accessibility and low actuation effort are critical [1,16], as well as industrial inspection and repair tasks in confined environments such as aircraft engines or pipelines [12]. In this study, the trade-off between the two objectives is managed using a Pareto-based multi-objective genetic algorithm (MOGA/NSGA-II) [22].

4.2. *Bi-objective optimization framework*

The bi-objective optimization problem is defined over a decision variable vector $\in R^n$, and aims to minimize the mechanical work $W(\xi)$ while maximizing the feasible static workspace $FSW(\xi)$. This can be expressed as:

$$ \underset{\xi\in R^n}{min}[W(\xi), -FSW(\xi)] \tag{27} $$

subject to:

$g_j(\xi) \le 0, (j = 1, \ldots, m)$ (geometric inequality constraints)

$h_l(\xi) = 0, (l = 1, \ldots, p)$(equality constraints, if any)

Here, $g_j(\xi)$ represents nonlinear geometric constraints, including bounds on tendon radii, angular offsets, and minimum tendon separation (e.g., Eqs. (31)–34). Equality constraints $h_l(\xi)$ includes any additional design relations enforced as equalities. The feasible design space is defined as:

$$ \Omega = \left\{ \xi \in R^n : g_j(\xi) \le 0, h_l(\xi) = 0 \right\} \tag{28} $$

A solution $\xi^* \in \Omega$ is Pareto-optimal if no other $\xi \in \Omega$ improves one objective without degrading at least one other.

4.2.1. *Objective 1: mechanical work*

The mechanical work is used here as a static effort metric to quantify the internal force and moment required to maintain a given configuration. Under the (PCC) assumption, it is computed as the sum of translational and rotational contributions at each vertebra:

$$ W(\xi) = C_1 = \sum_{i=1}^{n} \left[\left(\boldsymbol{F}_{net,i} \cdot \boldsymbol{po}_i \right) + \left(\boldsymbol{M}_{net,i} \cdot \boldsymbol{or}_i \right) \right] \tag{29} $$

where $\boldsymbol{F}_{net,i}$ and $\boldsymbol{M}_{net,i}$ are the net interna force and moment acting on the $(i)^{th}$ vertebra, n is the total number of vertebrae in the robot, and $\boldsymbol{po}_i$ and $\boldsymbol{or}_i$ are the corresponding global position and orientation vectors,

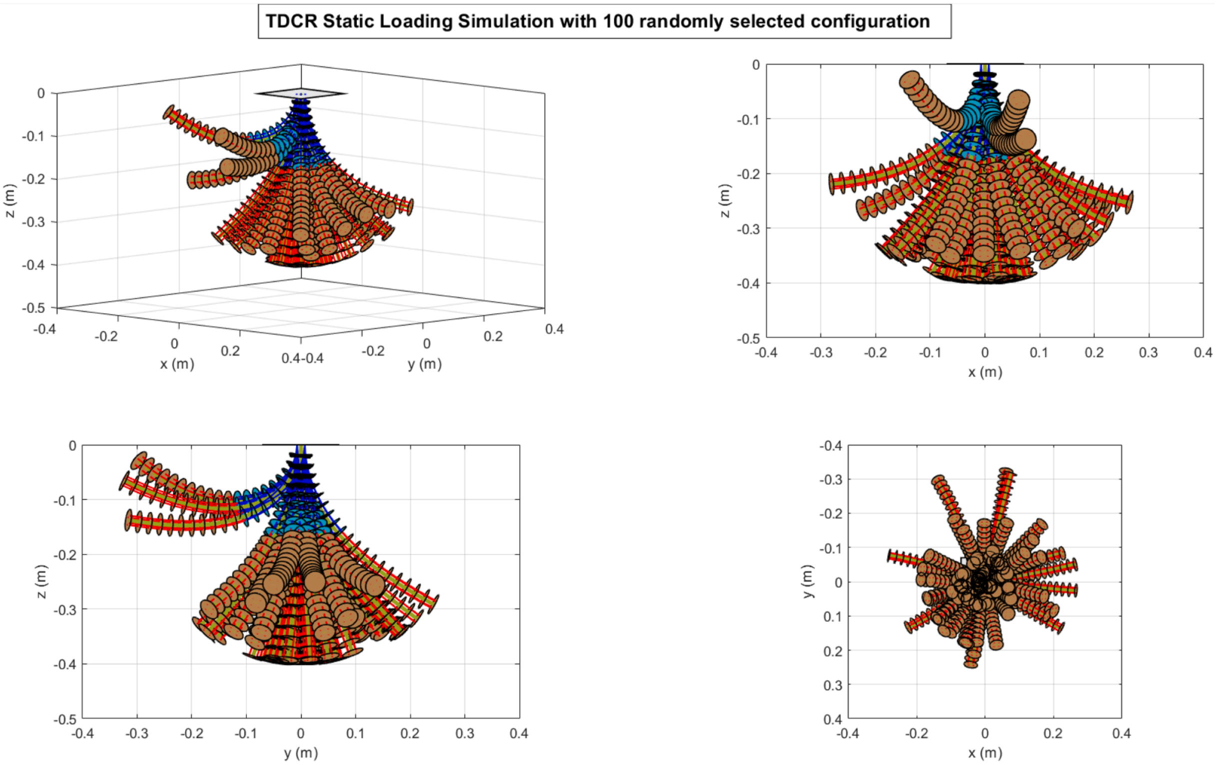

Fig. 5. End-effector positions under 100 randomized tendon force vectors, showing statistical coverage of the feasible workspace.

respectively [26].

4.2.2. Objective 2: feasible static workspace

The feasible static workspace (FSW) refers to the set of maximum reachable end-effector positions under static equilibrium conditions, evaluated using a fixed set of randomized tendon force samples [25]. For each design ξ, the robot tip position $\boldsymbol{P}_{\boldsymbol{n}}^{(\boldsymbol{L})}(\boldsymbol{\xi})$ is computed under the $(L)^{th}$ force sample. To quantify reachability, FSW is defined as the maximum squared euclidean norm of the tip positions. This formulation can be expressed as follows:

$$\begin{aligned} &FSW(\xi) = C_2 = \max_{L=1,\ldots,N} \boldsymbol{P}_{\boldsymbol{n}}^{(\boldsymbol{L})}(\boldsymbol{\xi})^2 \\ &s.t. \quad \Theta(\mathscr{F},\mathscr{S}) = 0 \\ &\xi_i^l \le \xi_i \le \xi_i^u \end{aligned} \tag{30}$$

Here, ξ denotes the set of design variables, including the radial tendon placements and angular offset, constrained by lower and upper bounds ξ_i^l and ξ_i^u, respectively. The function $\Theta(\mathscr{F},\mathscr{S})$, defined in Eq. (30), represents the TDCR's kineto-static model represented in Section 2, which depends on the tendon forces $\mathscr{F}$ and configuration parameters $\mathscr{S}$, including curvatures about the local x- and y-axes and twist about

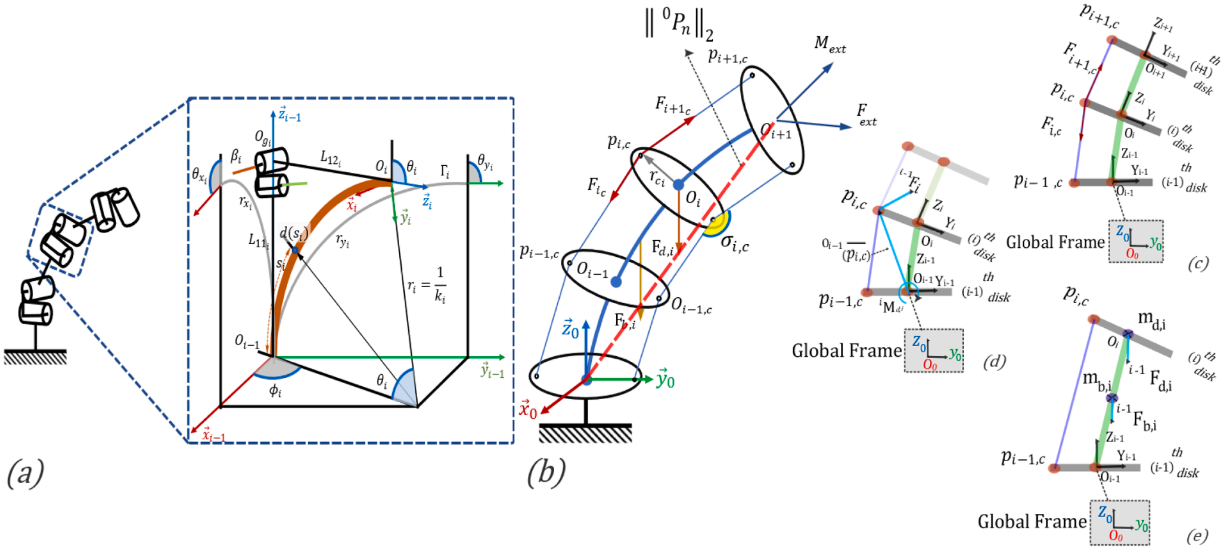

Fig. 6. (a) Subsegment kinematic diagram (b) Continuum robot pattern (c) Inter-Vertebral actuating forces applied on $\boldsymbol{i^{th}}$ disk (d) Actuating moment on $\boldsymbol{i^{th}}$ disk by resultant of inter-vertebral actuating forces (e) Disk and backbone masses and gravity forces for $\boldsymbol{i^{th}}$ vertebra.

the z-axis. To evaluate this objective, randomized tendon forces are sampled uniformly from [0,1],as detailed in Section 3. For each force sample, the kineto-static model is solved to compute the tip position $\boldsymbol{P}_n$, which defines the FSW metric (see Fig. 6(b)). This formulation offers a consistent and computationally efficient reachability measure that captures the effect of tendon actuation variability on end-effector extension. It enables the optimization process to evaluate design performance under diverse actuation conditions without requiring exhaustive volumetric workspace mapping.

In this study, the feasible static workspace (FSW) emphasizes the statically realizable reachability of the robot rather than its purely geometric range. The use of the maximum squared Euclidean norm directly incorporates tendon-force limits, external loading, and backbone stiffness constraints (Section 3.2), ensuring that only equilibrium-satisfying configurations are considered feasible. Although the convex-hull volume of reachable points could provide a broader geometric envelope, it would include configurations that violate static equilibrium or exceed actuation limits, potentially overestimating the effective workspace. The squared-norm formulation therefore offers a physically consistent, computationally tractable, and optimization-compatible metric well suited for integration within the multi-objective genetic algorithm framework used in this study.

4.3. Constraints

The optimization process is subject to a set of geometric constraints that ensure the physical feasibility and manufacturability of the tendon routing in the TDCR.

- Radial Tendon Spacing Constraints

The radial distance from the center of each vertebra to the tendon guide hole in segment m (where $m = 1, 2$) must lie within allowable physical limits:

$$r_c \le r_m \le r_d, \; m = 1, 2 \tag{31}$$

Here, r_c is the minimum inner radius that ensures clearance from the backbone, and r_d is the maximum outer radius to avoid tendon interference with the outer sheath [8]. A larger r_m improves mechanical leverage (torque arm) but increases frictional losses, representing a design trade-off.

- Angular Offset Constraints

To avoid collision between tendons and maintain structural symmetry, the angular offset α between corresponding tendon routes in adjacent segments must satisfy:

$$\alpha_{min} \le \alpha \le \alpha_{max} \tag{32}$$

Based on empirical studies [9], $\alpha_{min} = 30^{\circ}$ is recommended to prevent tendon overlap during significant bending motions. Higher angular offsets, while beneficial for expanding the reachable workspace (Section 5, Figs. 14–16), may introduce asymmetric loading, resulting in uneven bending stiffness and unbalanced internal moments [6,7].

- Nonlinear Tendon Interference Constraint

The distance between adjacent tendon routing holes, shown in Fig. 4, is determined from geometry using the law of cosines as:

$$d = \sqrt{r_1^2 + r_2^2 - 2r_1r_2\cos\alpha} \tag{33}$$

To ensure a minimum center-to-center separation and prevent physical overlap between tendon channels, a nonlinear inequality constraint is imposed:

$$d \ge \frac{1}{2}(d_1 + d_2) + d_t \tag{34}$$

where d_t is the minimum required edge-to-edge distance between any two tendon channels and $d_1$and d_2 are the tendon guide hole diameters in each segment. This constraint enforces geometric feasibility by ensuring that tendons remain physically separated throughout all admissible configurations, thereby maintaining structural integrity and avoiding mechanical interference.

5. Results and discussion

This section presents the computational setup and optimization results using a two-segment TDCR. The geometric and physical specifications used in the computation are summarized in Table 1, forming the foundation for modeling tendon behavior and actuation dynamics.

The optimization aimed to identify a set of Pareto-optimal tendon configurations that balance mechanical work C_1 and feasible static workspace C_2, as defined in Eqs. (29) and (30), respectively. While the optimization process minimizes mechanical work and maximizes workspace, the results are visualized by plotting the inverse of mechanical work on the horizontal axis and workspace on the vertical axis. Constraints (Eqs. (31)–(34)) were enforced to ensure geometric feasibility throughout the design space. To ensure robustness, 100 randomized tendon force samples ($\boldsymbol{F} \in \mathbb{R}^8$) were drawn uniformly from the interval [0,1] and applied consistently across independent optimization runs. Robustness here reflects the statistical representativeness of the FSW, ensured by these 100 randomized tendon force samples, which capture a comprehensive distribution of achievable configurations across optimization iterations. Representative Pareto fronts are presented in Figs. 7 and 8, and the main parameters of the Multi-Objective Genetic Algorithm (MOGA) are summarized in Table 2.

Each tendon force configuration was optimized independently, resulting in a diverse set of Pareto front optimal designs. To extract actionable design trends, the angular offset α defined as the angle between corresponding tendons in adjacent segments was discretized in 5° intervals. For each α range, relevant data points were filtered and statistically analyzed. Table 3 presents the grouped descriptive statistics across α intervals, including the number of optimization samples, the mean and variance of tendon radial distances *(r_1, r_2)*, the average α, and the associated performance metrics: C_1 (inverse mechanical work) and C_2 (feasible static workspace).

Figs. 9–17 visualize the corresponding distribution patterns and performance trends. Notably, configurations with larger α angles ($\ge 30^{\circ}$) tend to exhibit lower mechanical work, expanded feasible workspace, and reduced variance in both objectives, indicating improved performance and design robustness through wider tendon spacing. (see Figs. 14–17, where $\alpha \ge 30^{\circ}$ is highlighted in blue).

In contrast, denser groupings below $\alpha = 30^{\circ}$, while more frequent in

Table 1
Geometric and physical specifications of the TDCR.

Name	Description	Value	Unit
n	Number of total spacer disks	$[7,7]$	–
L	Length of sections	$\left[141 \times 10^{-3};\ 141 \times 10^{-3}\right]$	*m*
r_d	Outer radius of spacer disks	24.7×10^{-3}	*m*
r_c	Inner radius of spacer disks	12.57×10^{-3}	*m*
d_1	Tendon guide hole diameters	1.5×10^{-3}	*m*
d_2	Tendon guide hole diameters	1.5×10^{-3}	*m*
d_t	Edge to edge distance between the tendon guide holes	1.5×10^{-3}	*m*
m_{disk}	Mass of each spacer disk	9.254×10^{-3}	*kg*
m_b	Mass of backbone	2.893×10^{-3}	*kg*
k_x	Compliance coefficient in x direction	0.43	*N.m*
k_y	Compliance coefficient in y direction	0.25	*N.m*

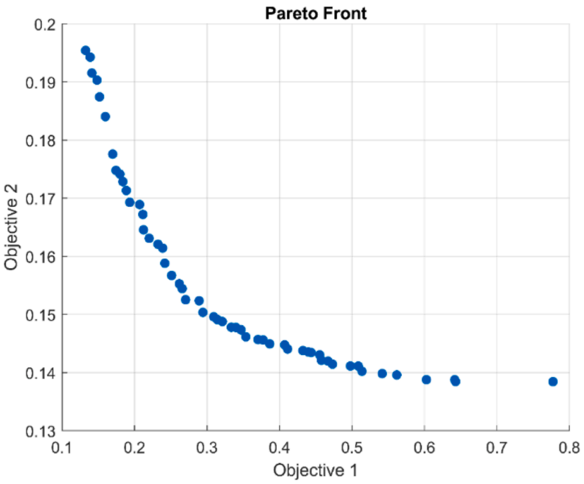

Fig. 7. Pareto front diagram, 14th iteration.

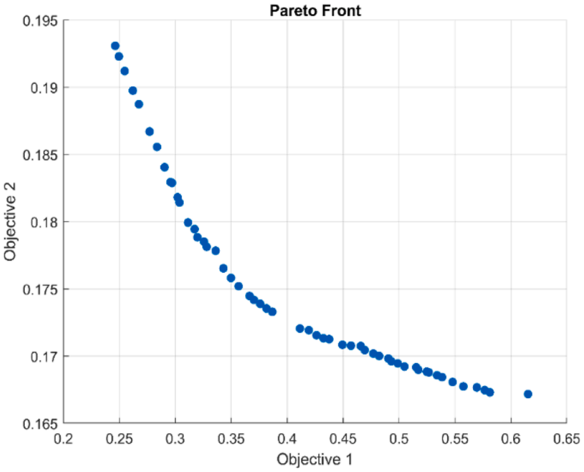

Fig. 8. Pareto front diagram, 61st iteration.

Table 2
MOGA optimization parameters.

Parameter	Description	Value
Population Size	Number of candidate solutions evaluated per generation	100
Number of Generations	Maximum number of iterations for the algorithm	10
Crossover Fraction	Proportion of individuals selected for crossover	0.8
Mutation Rate	Probability of mutation applied to offspring	0.2
Convergence Tolerance	Stopping criteria based on change in fitness value	1×10^{-6}
Tendon Force Samples	Number of randomized tendon force sets used for robustness	100
Force Distribution	Sampling method for tendon forces	Uniform in [0, 1]
Optimization Objectives	Objective 1: Mechanical Work (C_1) Objective 2: Feasible Static Workspace (C_2)	Bi-objective
Design Variables	Radial tendon positions (r_1, r_2), angular offset (α)	3 variables
External Load	Assumed tip load in simulation	F_{ext}= [0; 0; −0.1] N M_{ext}= [0; 0; 0] N·m

the solution space (see Fig.9), are less viable due to increased risk of tendon interference and mechanical instability, as detailed in Section 4.3 and supported by the statistical analysis in Section 5.

As illustrated in Fig. 9, the number of Pareto-optimal configurations varies across angular offset intervals (α), with denser clusters occurring at smaller offsets ($\alpha < 30^\circ$) and fewer but still representative solutions emerging at larger offsets ($\alpha \geq 30^\circ$). This variation results from the nonlinear feasibility constraints inherent in the optimization process. Consequently, the descriptive statistics summarized in Table 3 (means and variances) are primarily intended to highlight overall design trends and convergence patterns rather than to serve as strict statistical comparisons between groups.

All candidate configurations were evaluated under the same set of 100 randomized tendon-force samples, ensuring consistent performance assessment. Furthermore, to verify that the observed performance improvements are not artifacts of unequal sample sizes, an unequal-variance (Welch's) ANOVA test was performed, confirming that the increases in mechanical efficiency and feasible static workspace for $\alpha \geq 30^\circ$ remain statistically significant ($p < 0.05$).

These trends validate the effectiveness of choosing larger angular offsets in tendon routing and inform the final prototype parameters.

On the other hand, the design space for $\alpha \geq 30^\circ$ contains a sufficient number of feasible and high-performing configurations, which are analysed in more detail below. Fig. 10 shows that the mean α value across discretized intervals exhibits a near-linear trend, indicating stable design behaviour. Fig. 11 demonstrates that the variance in α remains tightly bounded between 1.4° and 1.5°, highlighting α as a reliable design parameter. Fig. 12 presents the average tendon radial distances for each segment. Below 35°, r_1 is ~20 mm while r_2 is ~24 mm, suggesting higher torque demands in the second segment. These values tend to converge as α increases. Fig. 13 reveals a higher variance in r_1 than r_2, suggesting more flexibility in tendon placement within the first segment.

Figs. 14–17 summarize the performance metrics. The mean inverse mechanical work (C_1) improves with larger α as shown in Fig. 14, while Fig. 15 confirms decreasing variance in C_1, confirming that its behaviour remains stable across different α values. Fig. 16 illustrates that the feasible static workspace (C_2) expands with α, and Fig. 17 shows its variance also diminishes. Collectively, these trends validate those wider angular separations enhance both energy efficiency and reachable configurations with robust performance.

Based on the optimization results, the most effective configuration places the tendons in both segments at the maximum feasible radial distance from the vertebral centre. This setup is supported by both objective metrics: increased α-angle leads to reduced mechanical work and improved feasible static workspace coverage. These trends confirm that wider tendon spacing enhances both energy efficiency and reachable configurations.

However, angular offset selection is also constrained by practical considerations: (1) mechanical integration requirements, such as motor support placement at 45° intervals (see Fig. 2), and (2) tendon interference risks at $\alpha < 30^\circ$, as reported in [9]. Accordingly, and supported by the results in Fig. 12, the prototype design adopts an angular offset of 45° with tendon radii of r_1= 21 mm and $r_2 = 22.5$ mm (see Fig. 2(c)).

This final design configuration balances simulation-driven optimization with real-world manufacturing constraints. It will guide the construction of the physical prototype, providing a tangible realization of the optimized TDCR structure and setting the stage for future experimental validation.

6. Conclusion

This study proposed a comprehensive optimization framework based on a bi-objective formulation for the dimensional synthesis of tendon-driven continuum robots (TDCRs), focusing on a two-segment design with seven disks and four tendons per segment. The methodology integrated geometric modelling, kineto-static simulation, and multi-

Table 3
Categorizing design variable data in all optimization examples by $\boldsymbol{\alpha}$ range.

α range (deg)	Num. of Samples	mean r_1(mm)	mean r_2(mm)	mean α(deg)	mean C_1(J^{-1})	mean C_2 (mm)	var. r_1 (mm)	var. r_2 (mm)	var. α (deg)	var. C_1 (J^{-1})	var. C_2 (mm)
0 - 5	454	19.64	23.34	2.79	1.58	255.36	2.19	0.39	1.52	488.59	3.97
5 - 10	672	20.42	23.30	7.59	1.65	257.06	2.13	0.46	1.45	662.97	3.75
10 - 15	693	20.23	23.33	12.48	1.48	258.40	2.29	0.20	1.45	396.64	2.95
15 - 20	612	20.28	23.31	17.37	1.45	260.32	2.24	0.21	1.46	415.43	2.31
20 - 25	374	20.33	23.30	22.30	1.41	261.97	2.22	0.22	1.36	401.41	1.60
25 - 30	157	20.05	23.35	27.13	1.44	262.95	2.39	0.18	1.39	535.29	1.36
30 - 35	50	21.58	23.34	32.30	2.07	263.69	1.86	0.14	1.46	1255.66	0.85
35 - 40	37	22.81	23.23	37.22	3.35	264.06	0.63	0.23	1.60	1464.18	0.76
40 - 45	40	21.79	23.05	43.46	2.50	264.54	2.08	0.51	1.47	1467.40	0.30

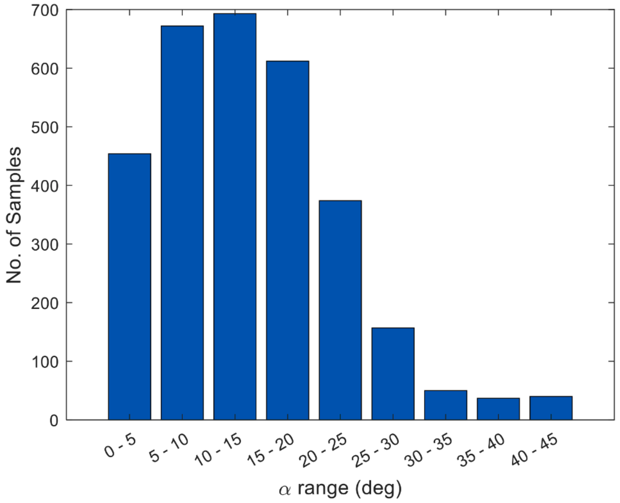

Fig. 9. Frequency histogram of the data as a function of $\boldsymbol{\alpha}$ – angle divisions.

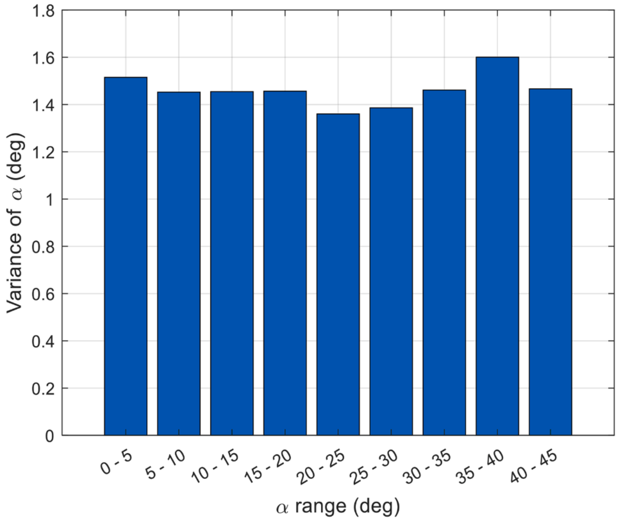

Fig. 11. Variance in the $\boldsymbol{\alpha}$ angle within each division.

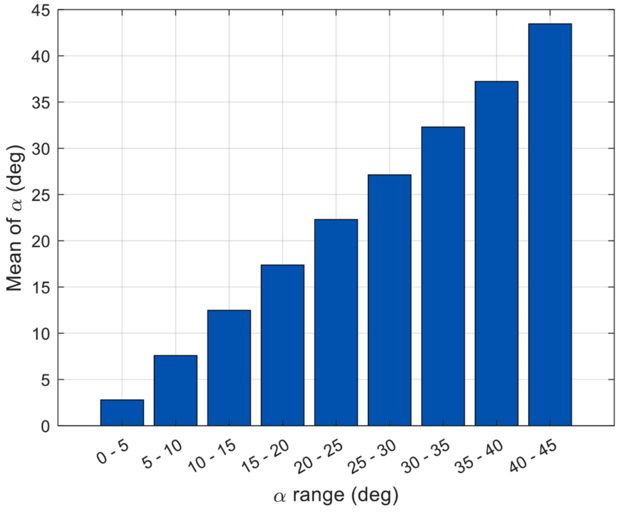

Fig. 10. Average $\boldsymbol{\alpha}$– angle for the optimal samples across the angular divisions.

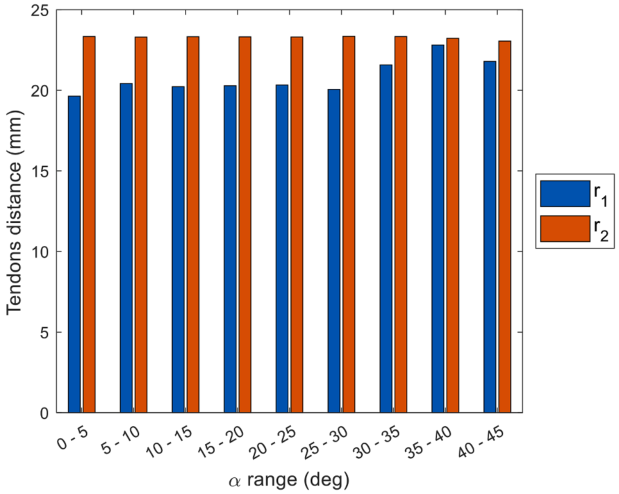

Fig. 12. Average radial distance of the tendons from the center of the vertebra for each segment.

objective optimization to address the trade-off between mechanical work and static workspace reachability.

A Pareto-front-based optimization using 100 randomized tendon force samples ensured a robust exploration of the design space, with key variables including radial tendon placement and angular offset, subject to geometric constraints such as tendon interference avoidance. The analysis revealed that larger angular offsets ($\alpha > 30^\circ$) and tendons positioned farther from the center ($r_1 = 21$ mm and $r_2 = 22.5$ mm) reduce the mechanical effort up to 30 % and lead to 3–5 % increase in reachable workspace, with the optimal design at $\alpha = 45^\circ$ meeting both theoretical and practical feasibility criteria. This configuration has been selected for a two-segment PA12 prototype, currently under bench-top testing to measure workspace boundaries and actuation forces, enabling future quantitative comparison with simulation results. While the optimal parameters are specific to this configuration, the framework's reliance on scalable geometric principles suggests potential

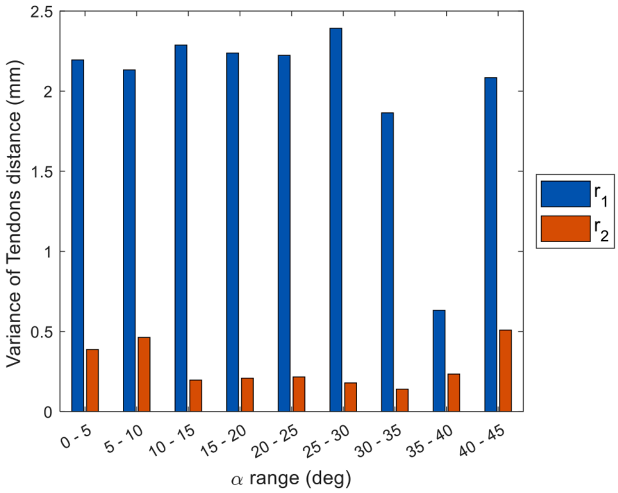

Fig. 13. Variance in radial tendon distances for each segment.

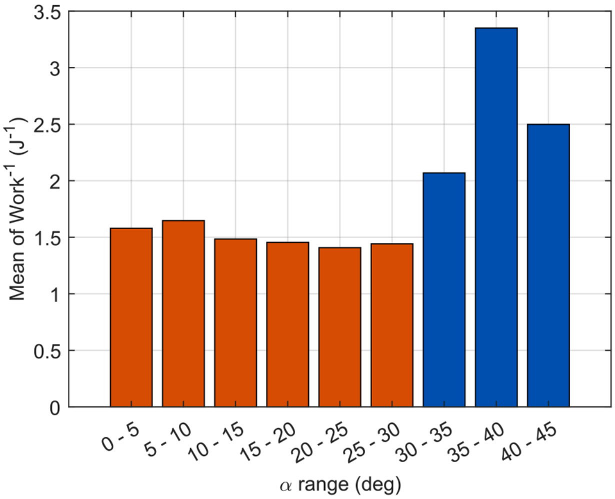

Fig. 14. Inverse work across the range of α-angle variations.

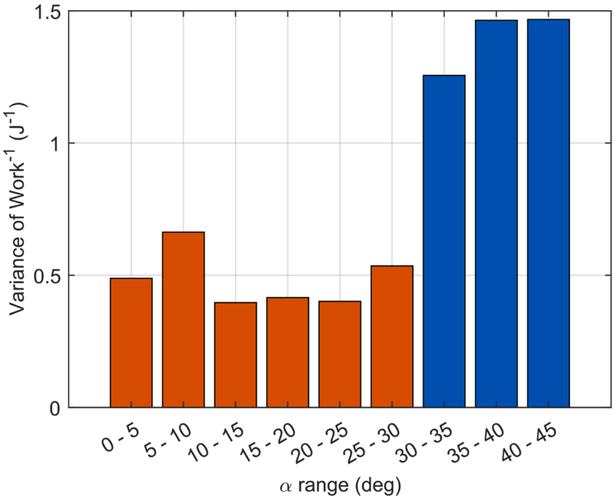

Fig. 15. Variance of inverse work across the range of α-angle variations.

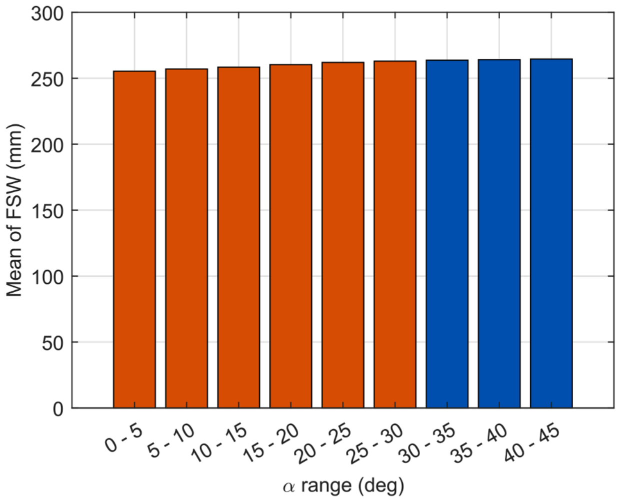

Fig. 16. Static feasible workspace across the range of α-angle variations.

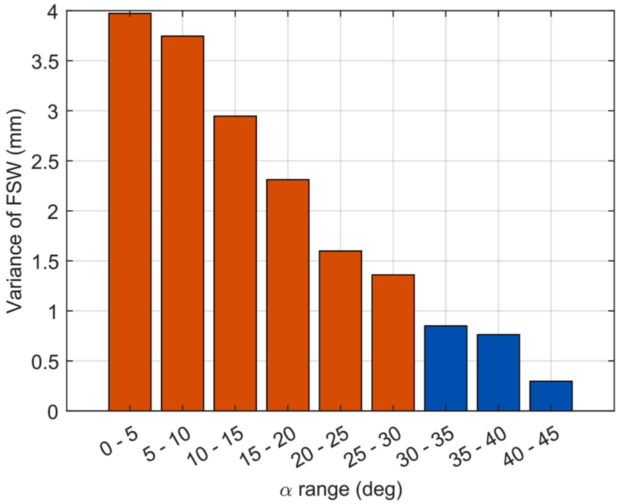

Fig. 17. Variance of static feasible workspace across the range of α-angle variations.

generalizability to TDCRs with different segment, disk, or tendon counts, a topic currently under investigation through simulations of three-segment designs. Ongoing work also targets experimental validation and future extensions, including dynamic control strategies and real-time adaptation, to further enhance applicability in medical and industrial environments.

CRediT authorship contribution statement

Mohammad Jabari: Writing – original draft, Visualization, Software, Methodology, Investigation, Conceptualization. **Carmen Visconte:** Writing – review & editing, Validation, Supervision, Methodology, Data curation, Conceptualization. **Giuseppe Quaglia:** Writing – review & editing, Supervision, Project administration, Conceptualization. **Med Amine Laribi:** Writing – review & editing, Validation, Supervision, Project administration, Methodology, Formal analysis, Conceptualization.

Declaration of competing interest

The authors declare the following financial interests/personal relationships which may be considered as potential competing interests:

Mohammad Jabari reports financial support was provided by PNRR-NGEU. This publication is part of the project PNRR-NGEU which has received funding from the MUR – DM 351/2022.If there are other authors, they declare that they have no known competing financial interests or personal relationships that could have appeared to influence the work reported in this paper.

Data availability

Data will be made available on request.

References

[1] J. Burgner-Kahrs, D.C. Rucker, H. Choset, Continuum robots for medical applications: a survey, IEEE Transact Robot. 31 (6) (2015) 1261–1280.

[2] Z. C. Mitros, S.M.H. Sadati, R. Henry, L. Da Cruz, C. Bergeles, From theoretical work to clinical translation: progress in concentric tube robots, Annu Rev. Control Robot. Auton. Syst. 5 (2022) 335–359, https://doi.org/10.1146/annurev-control-042920-014147.

[3] Y. Zhong, L. Hu, Y. Xu, Recent advances in design and actuation of continuum robots for medical applications, in: Actuators, 9, MDPI, 2020, p. 142.

[4] V.C. Anderson, R.C. Horn, T*ensor arm manipulator design*, Transact. ASME 67 (DE–57) (1967) 1–12.

[5] R.J. Webster, B.A. Jones, Design and kinematic modeling of constant curvature continuum robots: a review, Int. J. Robot. Res. 29 (13) (2010) 1661–1683.

[6] J. Starke, E. Amanov, M.T. Chikhaoui, J. Burgner-Kahrs, On the merits of helical tendon routing in continuum robots, in: 2017 IEEE/RSJ International Conference on Intelligent Robots and Systems (IROS), September 24, IEEE, 2017, pp. 6470–6476.

[7] E. Amanov, T.D. Nguyen, J. Burgner-Kahrs, Tendon-driven continuum robots with extensible sections A model-based evaluation of path-following motions, Int. J. Rob. Res. 40 (1) (2021) 7–23.

[8] R.M. Grassmann, P. Rao, Q. Peyron, J. Burgner-Kahrs, Fas—A fully actuated segment for tendon-driven continuum robots, Front. Robot. AI. 9 (2022) 873446.

[9] D. Barreiros, D.S. Shah, I.D. Walker, Configurable tendon routing for spatial follow-the-leader deployment, IEEE Robot. Autom. Lett. 4 (2) (2019) 1437–1444.

[10] J. Barrientos-Diez, M. Russo, X. Dong, D. Axinte, J. Kell, Asymmetric continuum robots, IEEE Robot. Autom. Lett. 8 (3) (2023) 1279–1286.

[11] N. Perugini, M. Russo, A monolithic tendon-driven continuum robot design for easy 3D printing and assembly, in: InThe International Conference of IFToMM ITALY, August 1, Springer Nature Switzerland, Cham, 2024, pp. 215–223.

[12] X. Dong, D. Axinte, D. Palmer, S. Cobos, M. Raffles, A. Rabani, J. Kell, Development of a slender continuum robotic system for on-wing inspection/repair of gas turbine engines, Robot. Comput. Integr. Manuf. 44 (2017) 218–229.

[13] D.B. Camarillo, C.F. Milne, C.R. Carlson, M.R. Zinn, J.K. Salisbury, Mechanics modeling of tendon-driven continuum manipulators, IEEE transactions on robotics 24 (6) (2008) 1262–1273.

[14] R.M. Grassmann, C. Shentu, T. Hamoda, P.T. Dewi, J. Burgner-Kahrs, Open continuum robotics–one actuation module to create them all, Front. Robot. AI. 11 (2024) 1272403.

[15] G. Böttcher, S. Lilge, J. Burgner-Kahrs, Design of a reconfigurable parallel continuum robot with tendon-actuated kinematic chains, IEEE Robot. Autom. Lett. 6 (2) (2021) 1272–1279.

[16] T. Kato, I. Okumura, S.E. Song, A.J. Golby, N. Hata, Tendon-driven continuum robot for endoscopic surgery: preclinical development and validation of a tension propagation model, IEEE/ASME Transact. Mechatron. 20 (5) (2014) 2252–2263.

[17] G. Runge, A. Raatz, A framework for the automated design and modelling of soft robotic systems, CIRP Ann. 66 (1) (2017) 9–12.

[18] J. Wang, C. Hu, G. Ning, L. Ma, X. Zhang, H. Liao, A novel miniature spring-based continuum manipulator for minimally invasive surgery: design and evaluation, IEEE/ASME Transact. Mechatron. 28 (5) (2023) 2716–2727.

[19] F. Qi, et al., Kinematics optimization and static analysis of a modular continuum robot used for minimally invasive surgery, Proceed. Instit. Mech. Eng., Part H: J. Eng. Med. 232 (2) (2018) 135–148.

[20] M. Jabari, C. Visconte, G. Quaglia, M.A. Laribi, Feasible static workspace optimization of tendon driven continuum robot based on euclidean norm, in: M. A. Laribi, G. Carbone, D. Pisla, S. Zeghloul (Eds.), New Trends in Medical and Service Robotics. MESROB 2025. Mechanisms and Machine Science, New Trends in Medical and Service Robotics. MESROB 2025. Mechanisms and Machine Science, 186, Springer, Cham, 2025, https://doi.org/10.1007/978-3-031-96081-9_49.

[21] Lotfavar, A., S. Hasanzadeh, and F. Janabi-Sharifi, *Cooperative Continuum Robots: concept, modeling, and workspace analysis.* 2018.

[22] The MathWorks, Inc., Global Optimization Toolbox User's Guide (Release R2024b), MathWorks, Natick, MA, 2024.

[23] D.E. Goldberg, Real-coded Genetic algorithms, Virtual Alphabets and Blocking, Citeseer, 1990.

[24] E. Gautreau, X. Bonnet, M.A. Laribi, Instrumented bio-inspired cable-driven compliant continuum robot: static modeling and experimental evaluation, Robotica (2024) 1–25.

[25] P. Rao, et al., How to model tendon-driven continuum robots and benchmark modelling performance, Front. Robot. AI. 7 (2021) 630245.

[26] P. Rao, O. Salzman, J. Burgner-Kahrs, Towards contact-aided motion planning for tendon-driven continuum robots, IEEE Robot. Autom. Lett. (2024).